Supporting Information

Platinum-Copper Nanowire Networks with Enhanced CO Tolerance Toward Methanol Oxidation Electrocatalysis

Shiyue Xing[a], Zhongliang Liu[a], Yingfang Jiang[a], Pinghui Tang[a], Jian Zhang[a], Jiatang Chen[b], Huihui Li*[a], and Chunzhong Li*[a]

a. Key Laboratory for Ultrafine Materials of Ministry of Education, School of Chemical Engineering, East China University of Science and Technology, Shanghai 200237, China.
b. Cornell High Energy Synchrotron Source, Wilson Laboratory, Cornell University, Ithaca, New York 14853, United States

1. Experimental Section

1.1 Chemicals.

The reagents required for the experiments were analytical grade. Chloroplatinic acid (H_2PtCl_6, 99.95%) was purchased from Adamas-beta, Copric chloride dihydrate ($CuCl_2 \cdot 2H_2O$, 98%) was purchased from Aladdin, sodium borohydride ($NaBH_{4,}$ 98%) was obtained from Sinopharm, absolute methanol (CH_3OH, ≥99.5%) was obtained from General-Reagent. Carbon black (Vulcan XC-72) was purchased from Cabot. Nafion (5 wt%) was purchased from Dupont. A commercial Pt/C (20 wt.%) catalyst was obtained from Johnson Matthey (London, UK). Deionized water (DIW, 18.2 MΩ cm^{-1}) was employed for the preparation of all solutions. All reagents were used without any further purification.

1.2 Preparation of $Pt_{42}Cu_{58}$ NWNs.

The synthesis of $Pt_{42}Cu_{58}$ NWNs was used with a one-pot wet-chemical protocol. Typically, 0.6 mL of 30 mM H_2PtCl_6 aqueous solution, 0.6 mL $CuCl_2 \cdot 2H_2O$ aqueous solution, and 150 mL of ultrapure water were well mixed in a 250 mL glass beaker. The mixture was put and stirred in a 30 °C water bath. After being stirred for about 5 min, 3.5 mL of 1.9 mg mL^{-1} $NaBH_4$ prepared freshly was quickly injected into the reaction solution by one shot, and the reaction was kept for 6 h under stirring. After the reaction, the products were collected by centrifugation and washed several times with water and ethanol. Finally, the products were dispersed in ethanol for further use. The $Pt_{67}Cu_{33}$ NWNs and $Pt_{19}Cu_{81}$ NWNs samples were prepared by similar methods, adjusting the feeding ratio of the metal precursor of Pt and Cu to 3:1 and 1:3, respectively. The actual metal loadings of the PtCu catalysts were measured by inductively coupled plasma-optical emission spectrometry (ICP-OES).

1.3 Characterizations.

Scanning electron microscopy (SEM) was performed using a Hitachi S-3400N (Hitachi, Tokyo, Japan) with an accelerating voltage range from 0.3 to 30 kV. Transmission electron microscopy (TEM) and high-resolution transmission electron microscopy (HR-TEM) were performed using FEI Talos F200X. Scanning TEM (STEM), STEM-energy dispersive X-ray spectroscopy (STEM-EDX) line-scanning, and elemental mapping characterization were used to further confirm the nanostructures, morphologies, and elemental distributions of the catalysts (FEI Talos F200X). X-ray diffraction (XRD) patterns of the synthesized catalysts were acquired by using a Rigaku SmartLab SE with Cu Kα as the X-ray source (40 mA, 40 kV, λ= 0.15406 nm). X-ray photoelectron spectroscopy (XPS) tests (Thermo Scientific K-Alpha with monochromatic) were used to collect the XPS spectra of the catalysts. Synchrotron X-ray absorption spectroscopy spectra were collected at the BL14W1 beamline of the Shanghai Synchrotron Radiation Facility (SSRF), and the corresponding data were analyzed using Athena software (ver. 0.9.26). The extended X-ray absorption fine structure (EXAFS) data fitting was performed using Artemis software[1]. Agilent 5800 ICP-OES Inductively Coupled Plasma Optical Emission Spectrometry (ICP-OES), Agilent (US), 5800 ICP-OES was used. In-situ attenuated total reflectance Fourier transform infrared (ATR-FTIR) spectroscopy measurements were conducted with a Thermo-Fisher Nicolet iS20 equipped with a liquid nitrogen-cooled MCT detector.

1.4 Electrochemical Measurements.

Before the electrocatalytic measurements, the homogeneous catalyst ink of electrocatalysts was fabricated by ultrasonically mixing 990 µL ethanol dispersion of the catalysts,10 µL 5 wt.% Nafion solution, and 1 mg carbon powder for about 30 min. For the electrochemical tests, the 5 µL of ink was dropped onto a clean glassy-carbon electrode (GCE, diameter: 3 mm) to prepare the working electrode, and the saturated Ag/AgCl and Pt foil (1cm×1cm) were served as reference and counter electrodes, respectively. Pt loadings were controlled at 8.5 µg/cm^2 for all samples. All the electrochemical measurements were performed on a CHI 760E (Chenhua, Shanghai) electrochemical workstation with a typical three-electrode configuration at ambient temperature, and all the recorded potentials were converted to the reversible hydrogen electrode (RHE). The cyclic voltammograms (CVs) were collected in N_2-saturated 0.1 M $HClO_4$ from -0.2 to 1 V (vs. Ag/AgCl) with a scan rate of 50 mV s^{-1}. The electrochemical active surface areas (ECSAs) were estimated according to the underpotentially deposited H (H_{upd}) methods. From the charge of the H_{upd} desorption peak in the recorded CVs, the ECSAs of catalysts were determined from one monolayer of hydrogen desorption on Pt with a criterion of 0.21 mC cm^{-2}.

The methanol oxidation reaction (MOR) polarization curves were obtained at the scan rate of 50 mV s^{-1} in N_2-saturated 0.1 M $HClO_4$ and 0.5 M methanol solution. Before MOR tests, the catalysts were activated by conducting the CVs to be stable in N_2-saturated 0.1 M $HClO_4$ at a sweep rate of 250 mV s^{-1}. The chronoamperometry (CA) measurements of MOR were conducted in 0.1 M $HClO_4$ and 0.5 M methanol solution at 0.6 V vs. Ag/AgCl. A linear sweep voltammetry (LSV) was implemented to record polarization curves for the methanol electro-oxidation reaction in N_2-saturated 0.1 M $HClO_4$ and 0.5 M methanol solution at 5 mV s^{-1}. For the CO stripping measurement, the working electrode was held at a constant potential of 0.1

V vs. RHE under a flow of CO bubbled into the N_2-saturated 0.1 M $HClO_4$ electrolyte for 10 min and then change CO to N_2 for another 20 min to absorb monolayer CO molecules. Afterward, the working electrode was recorded for two cycles at a scan rate of 50 mV s^{-1}.

1.5 Electrochemical in Situ ATR-FTIRS Experiments

In situ ATR-FTIRS measurements were performed on a Fourier transform infrared (FTIR) spectrometer equipped with an MCT/A detector (Thermo Fisher Nicolet iS50) with a resolution of 4 cm^{-1}. The tests were conducted in a spectroelectrochemical cell with a three-electrode configuration. The Au film was plated on Ge prism, which played a role in enhancing the FTIR signals. The catalyst ink was drop-casted on the Au film and naturally dried at room temperature. Ag/AgCl and Pt wire were used as the reference electrode and the counter electrode, respectively. The IR spectra were collected from 0.26 to 1.26 V vs. RHE in N_2-saturated 0.1 M $HClO_4$ + 0.5 M methanol.

1.6 The computing method of ECSA

The ECSA of Pt-based samples was calculated based on the following equation:

$$ECSA = \frac{Q}{m \times C} \tag{1}$$

Q is the charge collected in the hydrogen adsorption/desorption region, m is the weight of the Pt loading, and C is the charge required for monolayer adsorption of hydrogen on a Pt (210 μC cm^{-2}) surface.

1.7 The calculation of α and j_0

Tafel slope of all studied MOR electrocatalysts was determined from the Tafel plots, which were fitted by the Tafel equation on the following[2]:

$$\eta = blogj + a = \frac{2.3RT}{\alpha nF}logj - \frac{2.3RT}{\alpha nF}logj_0 \tag{2}$$

where R and T(K) present gas constant and absolute temperature, respectively; α denotes a charge transfer coefficient, F is a Faraday constant, and j_0 (mA cm^{-2}) is an exchange current.

1.8 The calculation of E_a

The activation energy (E_a) was calculated through the Arrhenius equation[3]:

$$k(T) = Ae^{-E_a/RT} \tag{3}$$

where k(T) and A are rate constant and a pre-exponential factor, respectively. R and T are gas constant and temperature, respectively. The apparent activation energy was achieved from the measured current density at different temperatures via Eq.(3)[3]:

$$E_{a(app)} = -2.303R\left[\frac{d\ln i}{d(1/T)}\right] \tag{4}$$

1.9 Estimation of strain from XRD

According to Bragg's law and the cell parameter formula of the fcc structure, the lattice paramter (a) can be obtained by the following equation[4-6]:

$$d_{h,k,l} = \frac{\lambda}{2sin\theta} \tag{5}$$

$$d_{h,k,l} = \frac{a}{(h^2 + k^2 + l^2)^{\frac{1}{2}}} \tag{6}$$

where $d_{h,k,l}$ indicates the interplanar spacing, λ and θ represent the X-ray wavelength ($\lambda = 0.15406\ nm$) and Bragg angle, respectively. In addition, a is the lattice parameter (Å) and h, k, l means the Miller indices. For the Pt (111) lattice, h = k = l = 1.

The strains of the Pt_xCu_y NWNs are further estimated using the equation (4) below[7, 8]:

$$s(Pt) = \frac{a_n - a_b}{a_b} \times 100\% \tag{7}$$

Where a_b is the lattice parameter of the pure Pt (that is, 3.923 Å; JCPDS no. 04-0802), and a_n is the lattice parameter of the corresponding Pt_xCu_y NWNs.

2.0 The calculation method of d-band centers

The d-band centers of Pt_xCu_y NWNs and commercial Pt/C were calculated from the following equation based on the valence band spectra:

$$d - band\ center = -\int_{-2eV}^{10eV} \frac{[binding\ energy(E)intensity(E)]dE}{\int_{-2eV}^{10eV} intensity(E)dE} \tag{8}$$

2.1 The calculation method of Pt 5d holes of the samples:

The number of Pt 5d holes in each sample are calculated by the whiteline areas (A_3, A_2) of Pt $L_{3,2}$ edges, utilizing the 2p-5d transition matrix elements of Pt[9].

$$A_3 = C_0 N_0 E_3 \left(R_{5d}^{2p_{3/2}}\right)^2 \left(\frac{6h_{5/2} + h_{3/2}}{15}\right) \tag{9}$$

$$A_2 = C_0 N_0 E_2 \left(R_{5d}^{2p_{1/2}}\right)^2 \left(\frac{h_{3/2}}{3}\right) \tag{10}$$

where $C_o = 4\pi^2\alpha/3$ and where α is the fine structure constant. N_0 is the atomic density of Pt, 1.12×10^{23} atoms cm^{-3}. E_3 and E_2 are the threshold energy of Pt L_3-edge (11 564 eV) and Pt L_2-edges (13 273 eV), respectively. $R_{5d}^{2p_{3/2}}$ and $R_{5d}^{2p_{1/2}}$ are the radial dipole-moment matrix elements for Pt $2p_{3/2}$ → 5d and $2p_{1/2}$ → 5d transitions. The two equations above can be rearranged to simplify the expressions of $h_{5/2}$ and $h_{3/2}$, as shown below:

$$h_{5/2} = \frac{1}{2C}(5\frac{E_2}{E_3}A_3 - A_2) \quad (11)$$

$$h_{3/2} = \frac{3}{C}(A_2) \quad (12)$$

where C is a constant (16.44) obtained by assuming the total number of Pt 5d holes to be 1. The total d-band holes (vacancies) can be calculated by the equation below:

$$h_T = h_{3/2} + h_{5/2} \quad (13)$$

The following figure shows the example of A_3 extraction for Pt foil, by firstly subtracting the Au L_3-edge (E_0 aligned with Pt; Au 5d states are known as fully filled, thus considered with no 2p-5d transition at both L_3 and L_2 edges[10]) from Pt L_3-edge; then conducting a fitting process to extract the whiteline (a pseudo-Voigt peak with 90% Lorentzian and 10% Gaussian). The L_3-edge whiteline area is then integrated to be A_3 (Fig. S7).

While the Pt L_2 edges were not measured for the Pt_xCu_y NWNs samples in this study, the A_2 can be extrapolated from the A_2-A_3 correlation, using the A_3 from Pt L_3 edges. The A_2-A_3 correlation is established by linearly fitting the A_3 and A_2 extracted from the Pt $L_{3,2}$ edges of standard Pt-Ni random alloys. The details of these alloys have been reported in literature [11]. Note that to provide reliable whiteline areas, the XAS of Pt-Ni alloys (collected in transmission mode) and Pt_xCu_y NWNs samples in this study were processed following the same procedures, as mentioned above (Fig. S8). This method is based on the fact that the Pt_xCu_y NWNs samples, Pt-Ni alloys, and Pt share a similar crystal structure (fcc).

The calculated results are shown in the following Table S3. Note that the total number of Pt 5d holes is assumed to be 1 to obtained the constant C (16.44) in the equation for 5d hole calculations. Δh is the change in the number of holes (negative means more electron) compared with pure Pt.

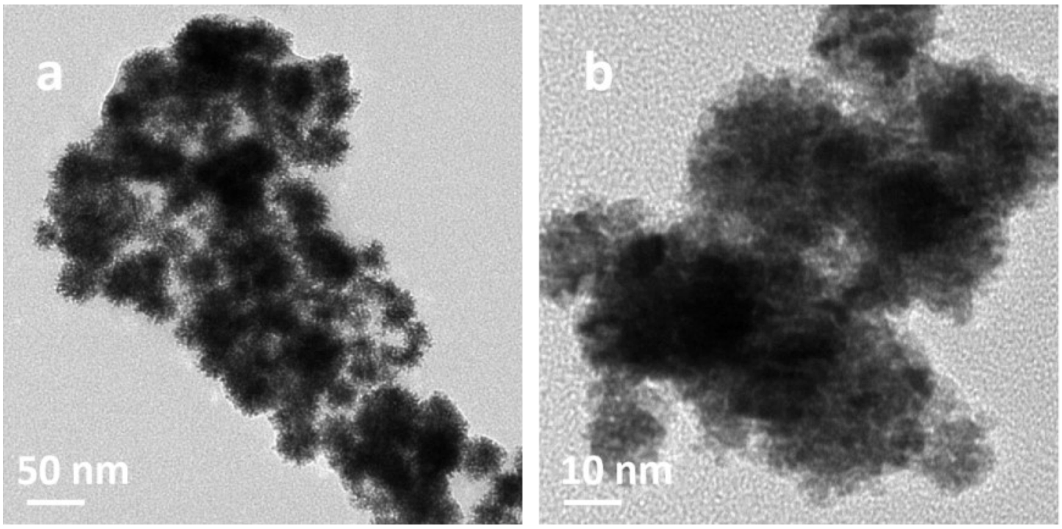

Figure S1. TEM images of the products from the reaction with the same conditions used in the synthesis of $Pt_{42}Cu_{58}$ NWNs, except for the reduction change by N_2H_4.

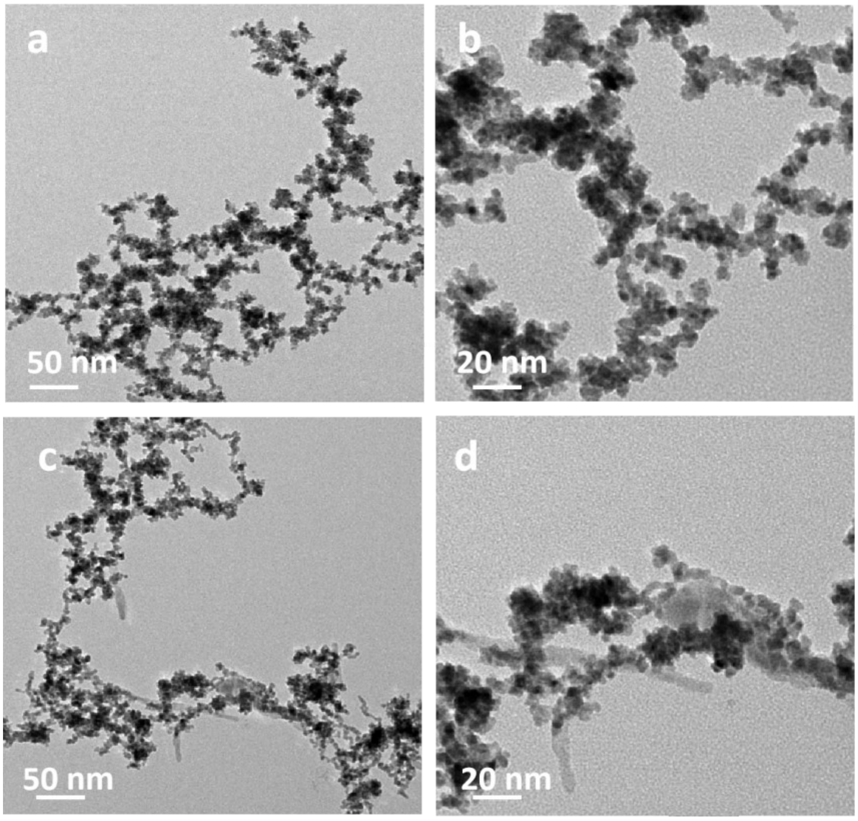

Figure S2. TEM images of the products from the reaction with the same conditions used in the synthesis of $Pt_{42}Cu_{58}$, but under the different reaction temperatures (a, b) 50 ℃; and (c, d) 70 ℃.

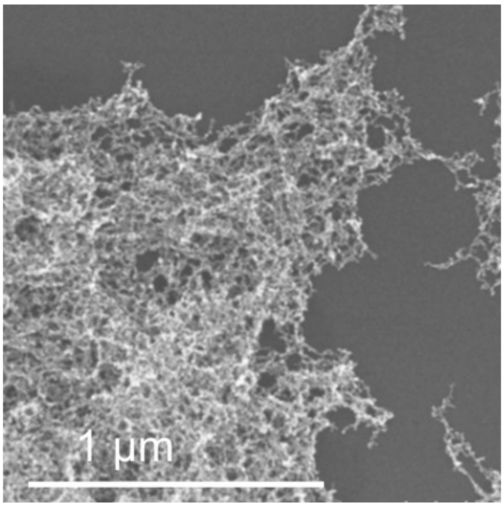

Figure S3. SEM images of $Pt_{42}Cu_{58}$ NWNs.

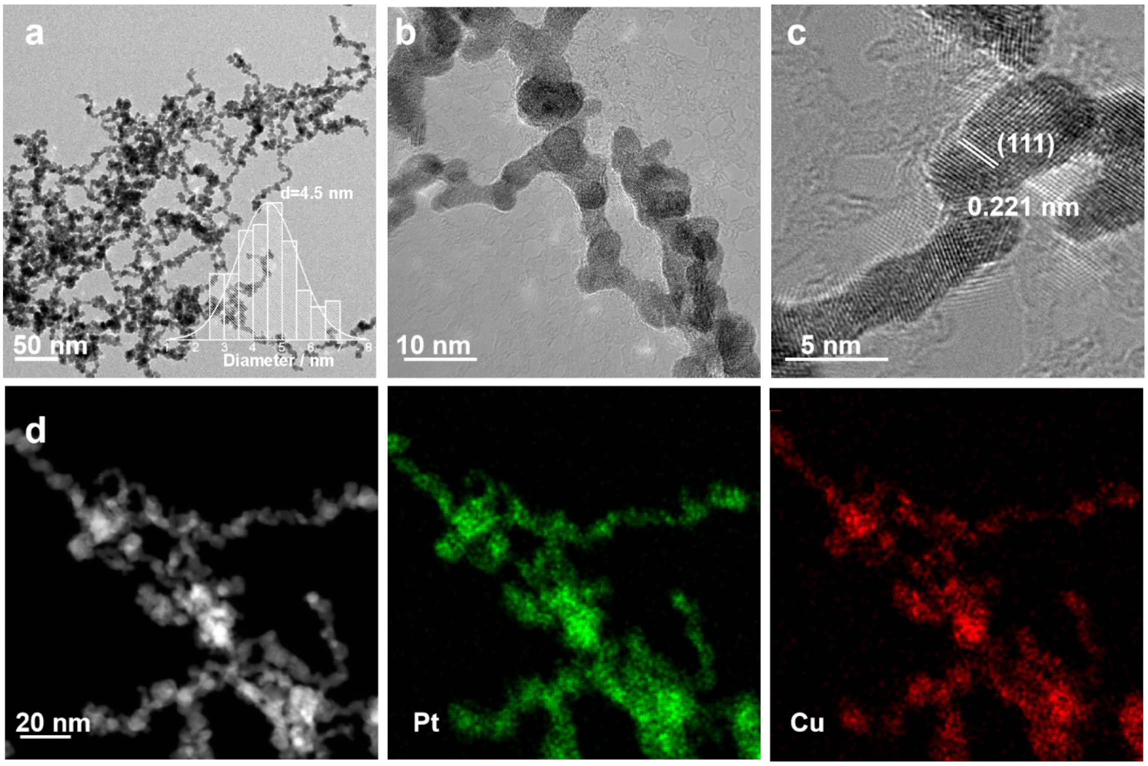

Figure S4. TEM image of $Pt_{67}Cu_{33}$ NWNs.

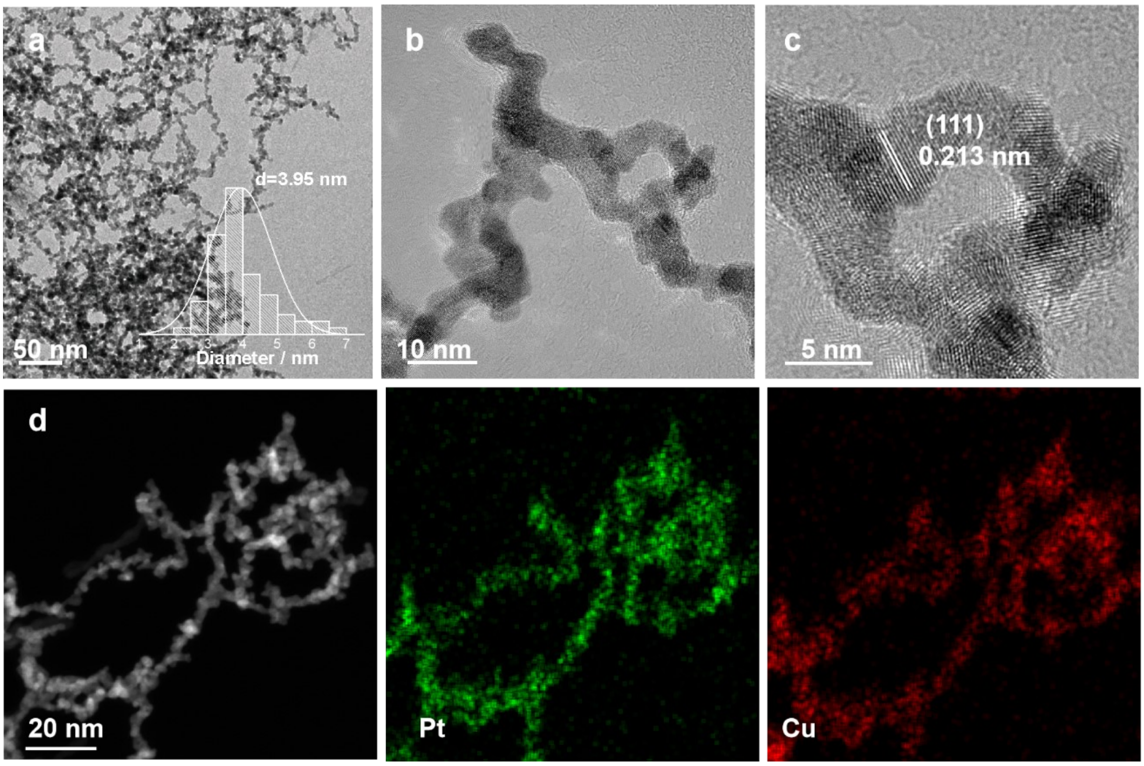

Figure S5. TEM image of $Pt_{19}Cu_{81}$ NWNs.

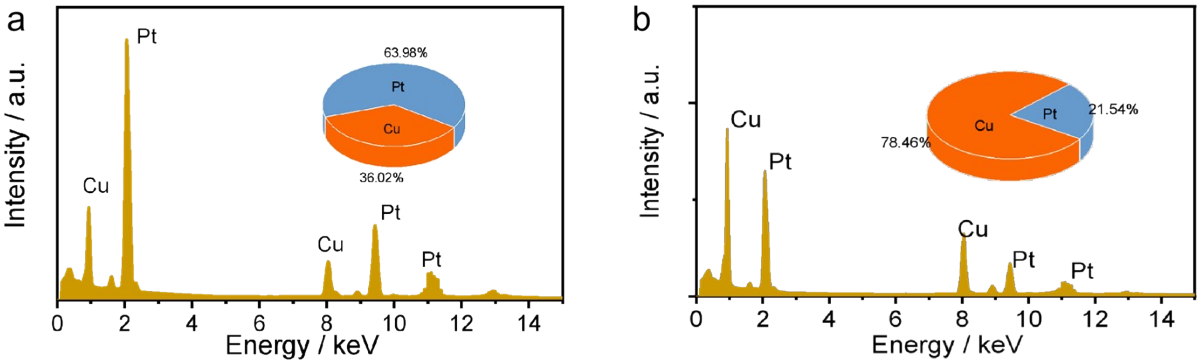

Figure S6. EDS of $Pt_{67}Cu_{33}$ NWNs and $Pt_{19}Cu_{81}$ NWNs.

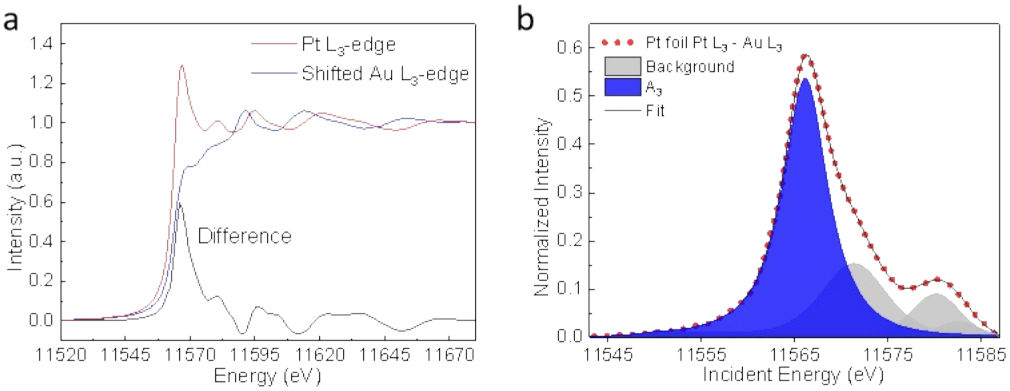

Figure S7. A_3 parameter extraction protocol for Pt foil through Pt L_3-edge analysis. (a) Background-subtracted spectrum after removing Au contribution; (b) Integrated area under whiteline defining A_3 value.

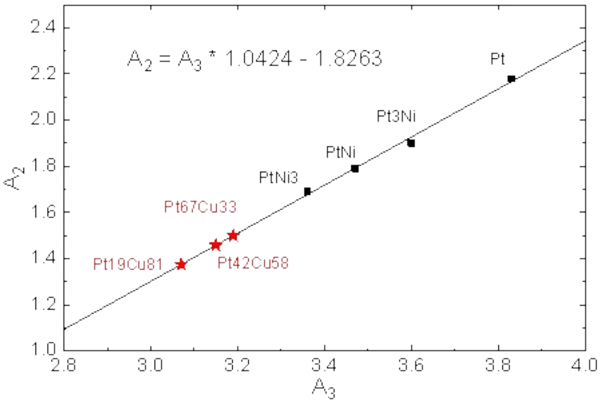

Figure S8. Linear correlation between A_2 and A_3 parameters derived from Pt L3,2-edges of standard Pt–Ni random alloys.

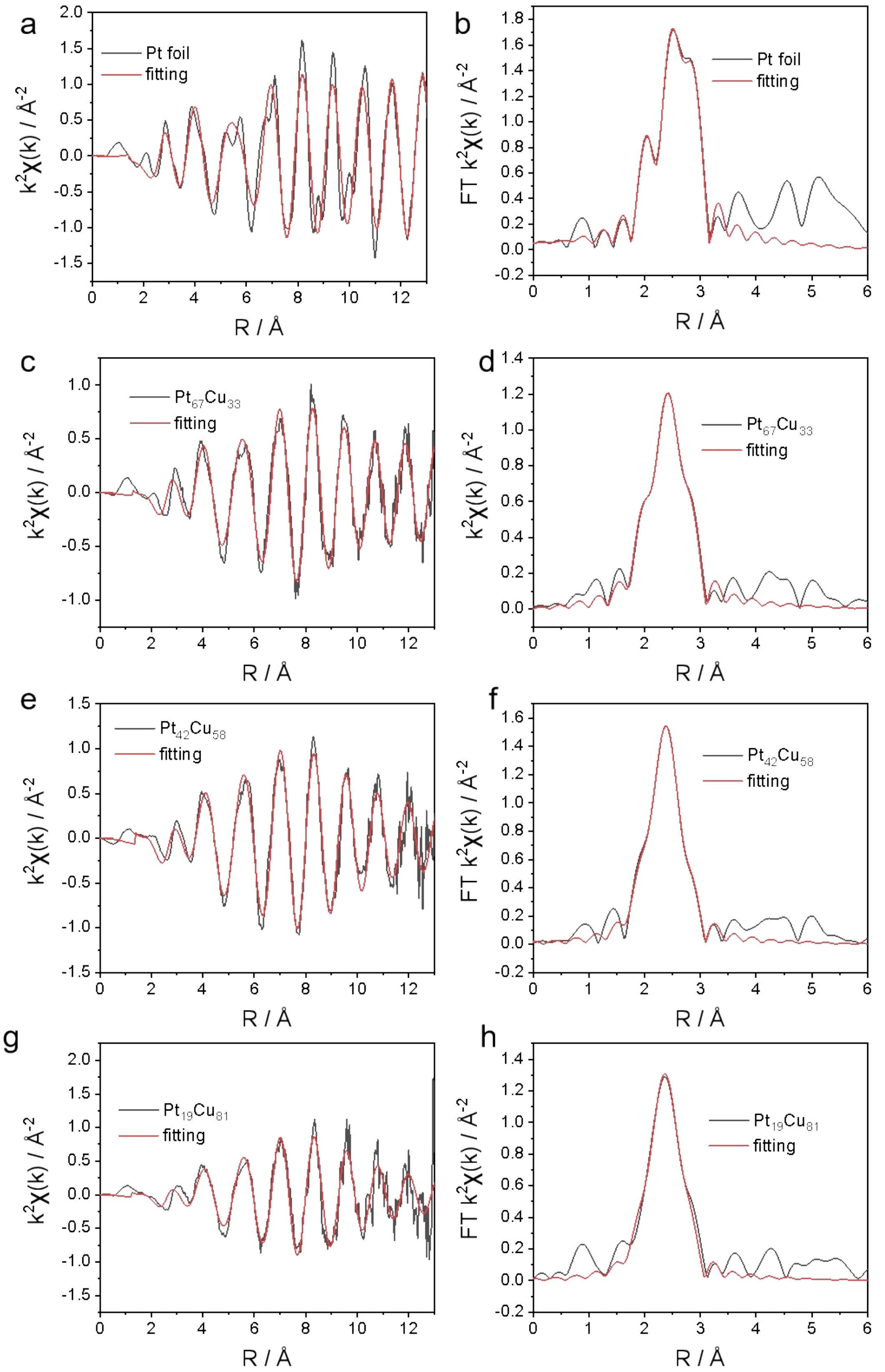

Figure S9. Experimental and fit data of Pt L_3-edge FT-EXAFS spectra in K space and R space for (a, b) Pt foil, (c, d) $Pt_{67}Cu_{33}$ NWNs, (e, f) $Pt_{42}Cu_{58}$ NWNs and (g, h) $Pt_{19}Cu_{81}$ NWNs.

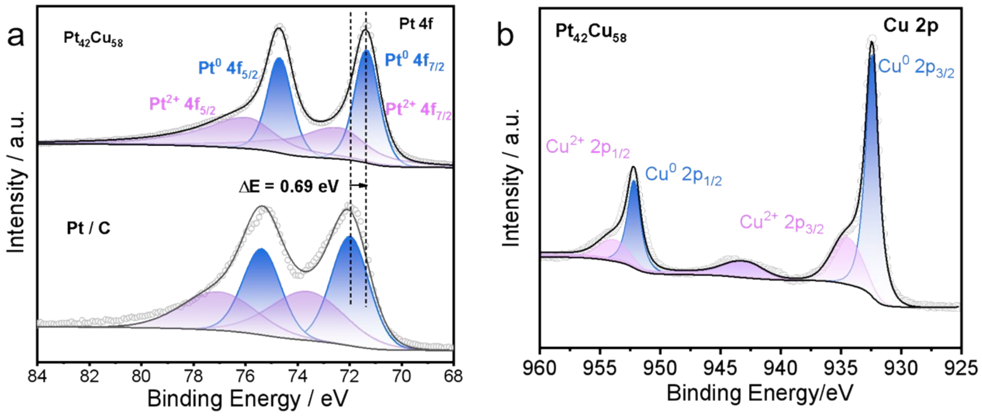

Figure S10. XPS images of $Pt_{42}Cu_{58}$ NWNs.

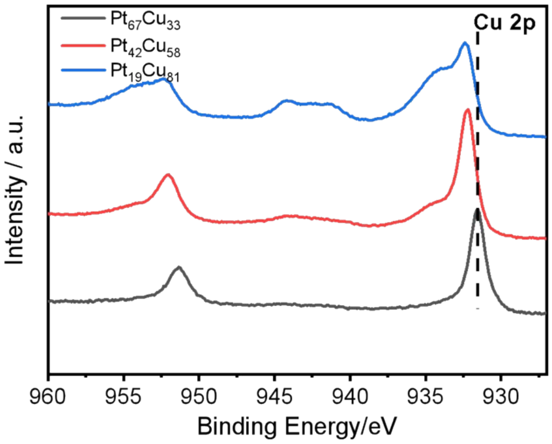

Figure S11. XPS images of Cu 2p of PtCu NWNs.

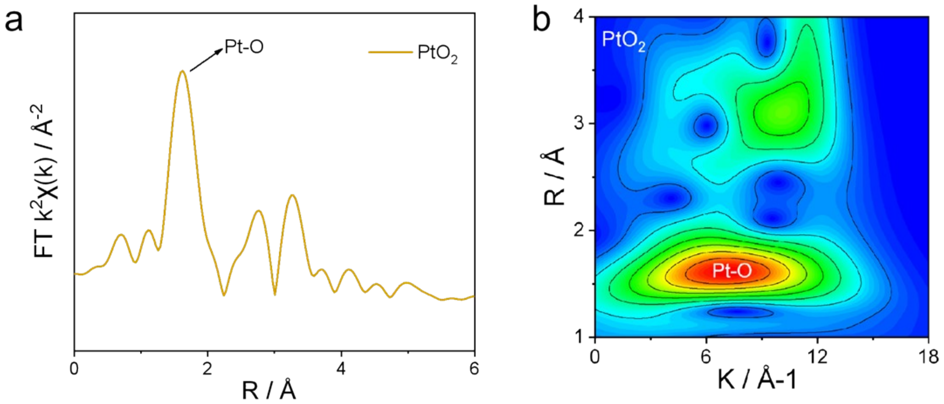

Figure S12. a) FT-EXAFS and b) EXAFS wavelet transformation (WT) plots of PtO_2.

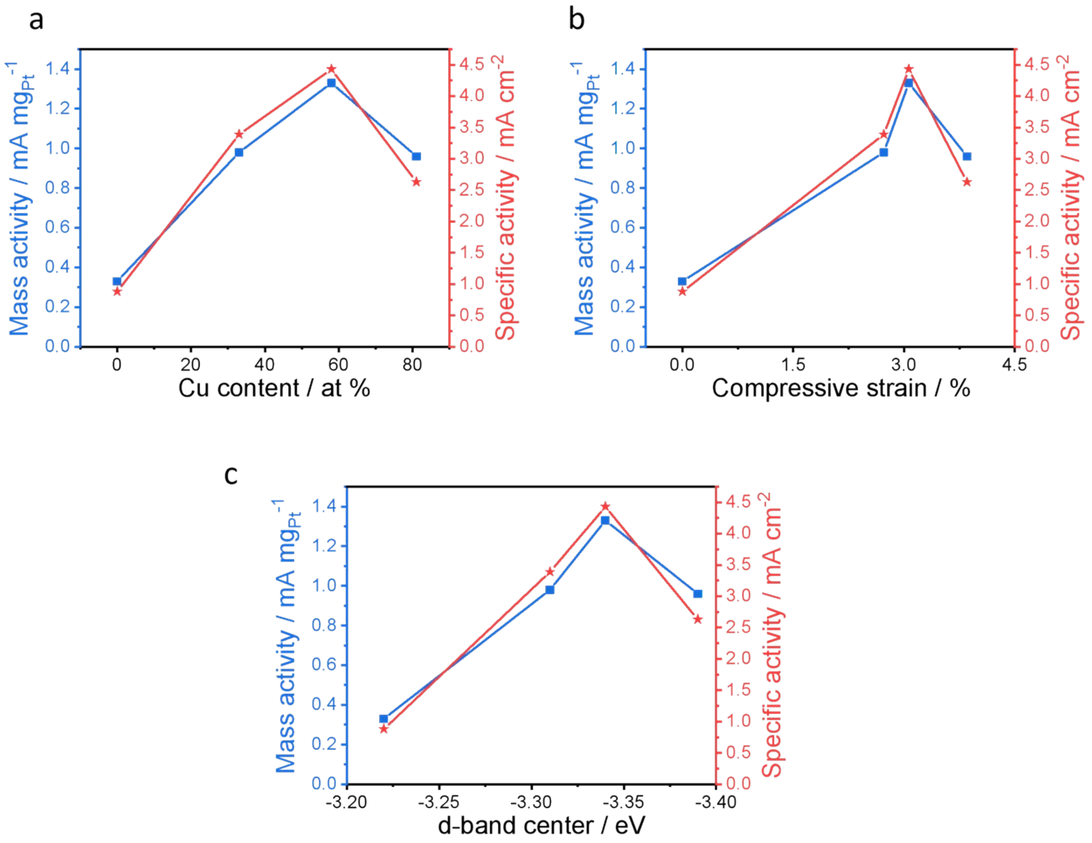

Figure S13. Relationships between the MOR activity and the a) Cu component, b) compressive strain, and c) d-band center of different catalysts.

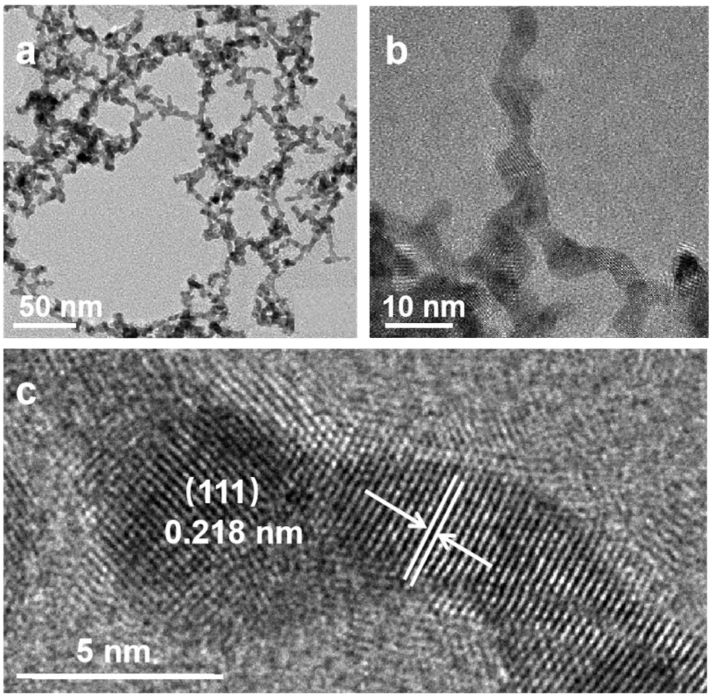

Figure S14. TEM images of $Pt_{42}Cu_{58}$ NWNs after durability test.

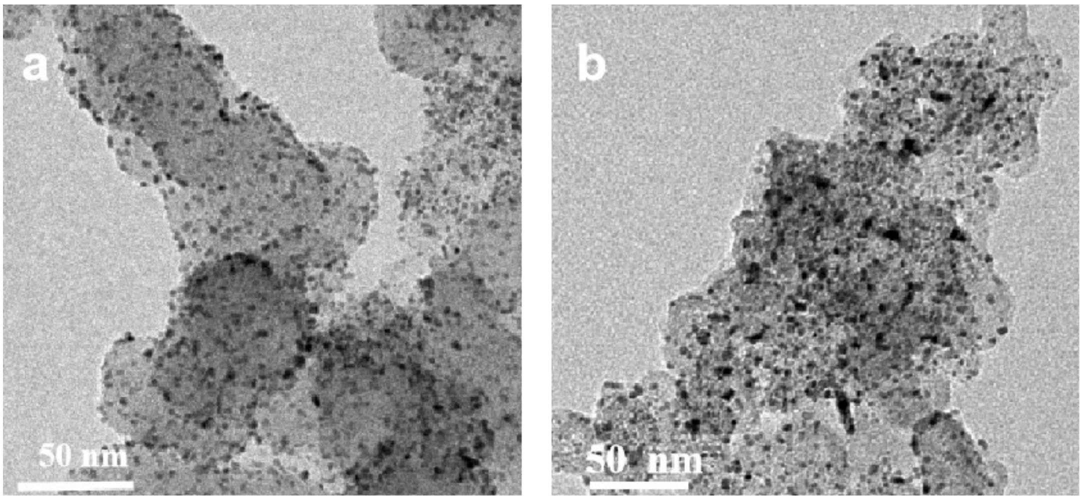

Figure S15. TEM images of commercial Pt/C catalysts before (a) and after (b) durability test.

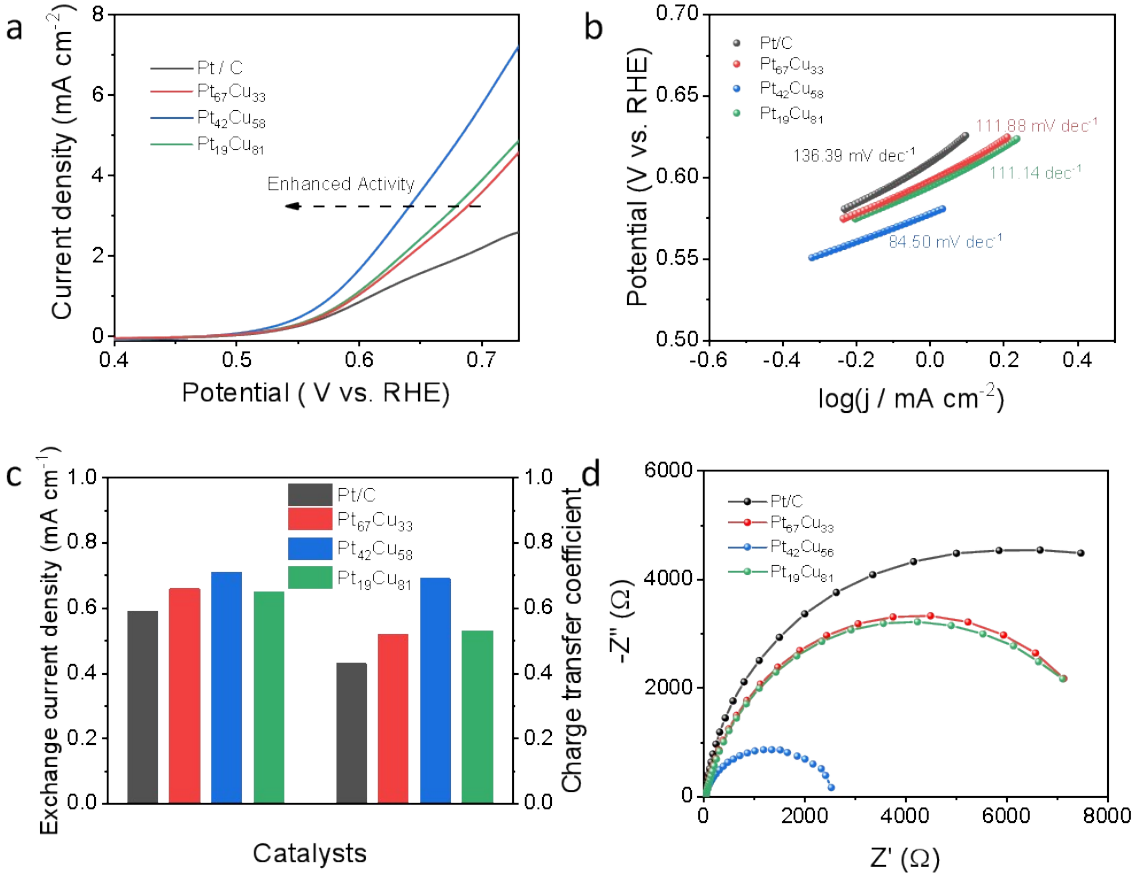

Figure S16. (a) LSV curves, (b) corresponding Tafel plots in N_2-saturated 0.1 M $HClO_4$ containing 0.5 M methanol solution electrolyte at a scan rate of 5 mV s^{-1}, (c) exchange current density and charge transfer coefficient of all samples, and (d) EIS Nyquist plots of all samples in the frequency range of 0.1–10^5 Hz at 0.56 V vs. RHE.

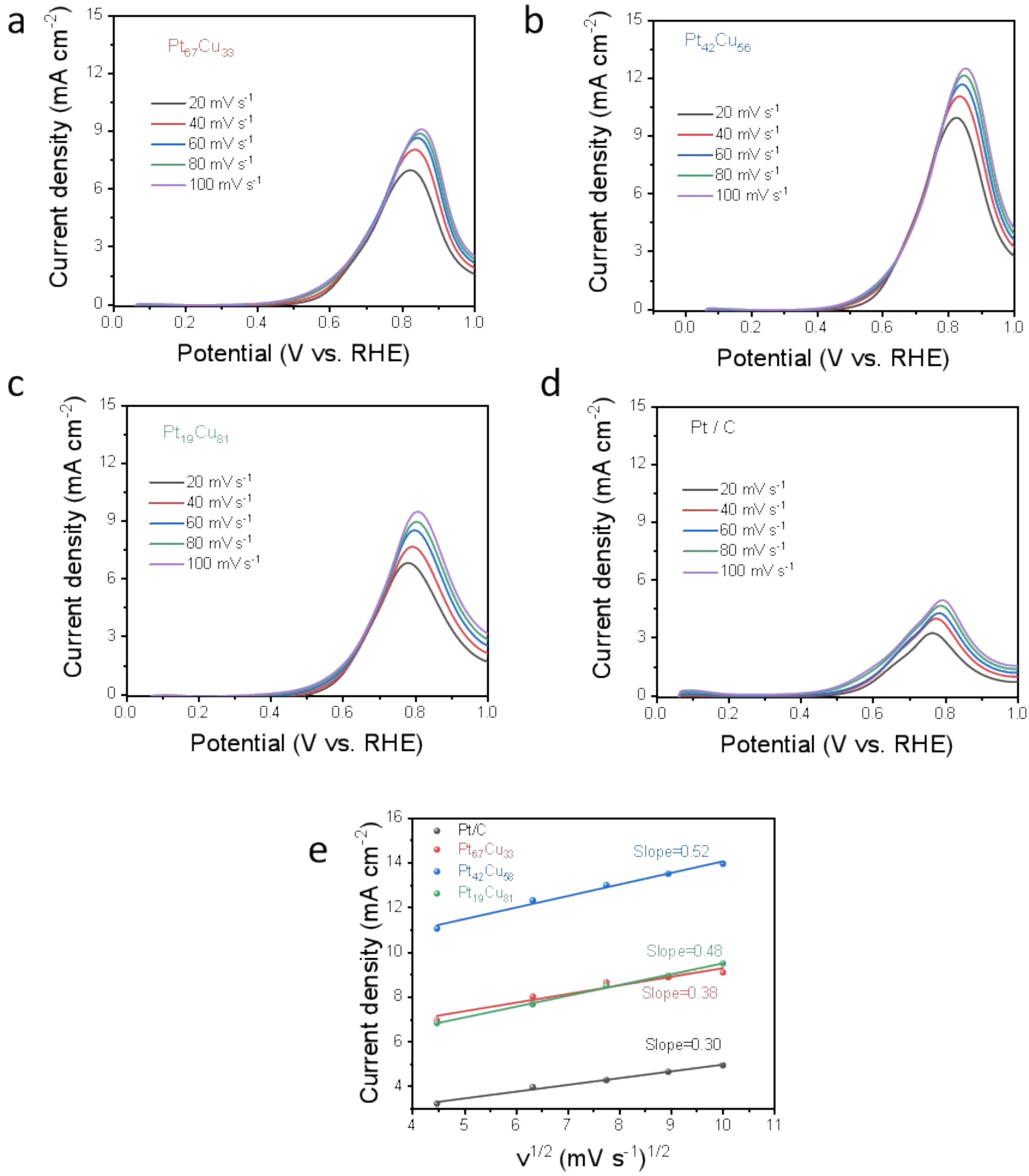

Figure S17. (a–d) Anodic peak current density at different scan rates (20, 40, 60, 80, and 100 mV s^{-1}), (e) corresponding linear relationship between the anodic peak current density and the square root of scan rates of all samples in N_2-saturated 0.1 M $HClO_4$ containing 0.5 M methanol solution electrolyte.

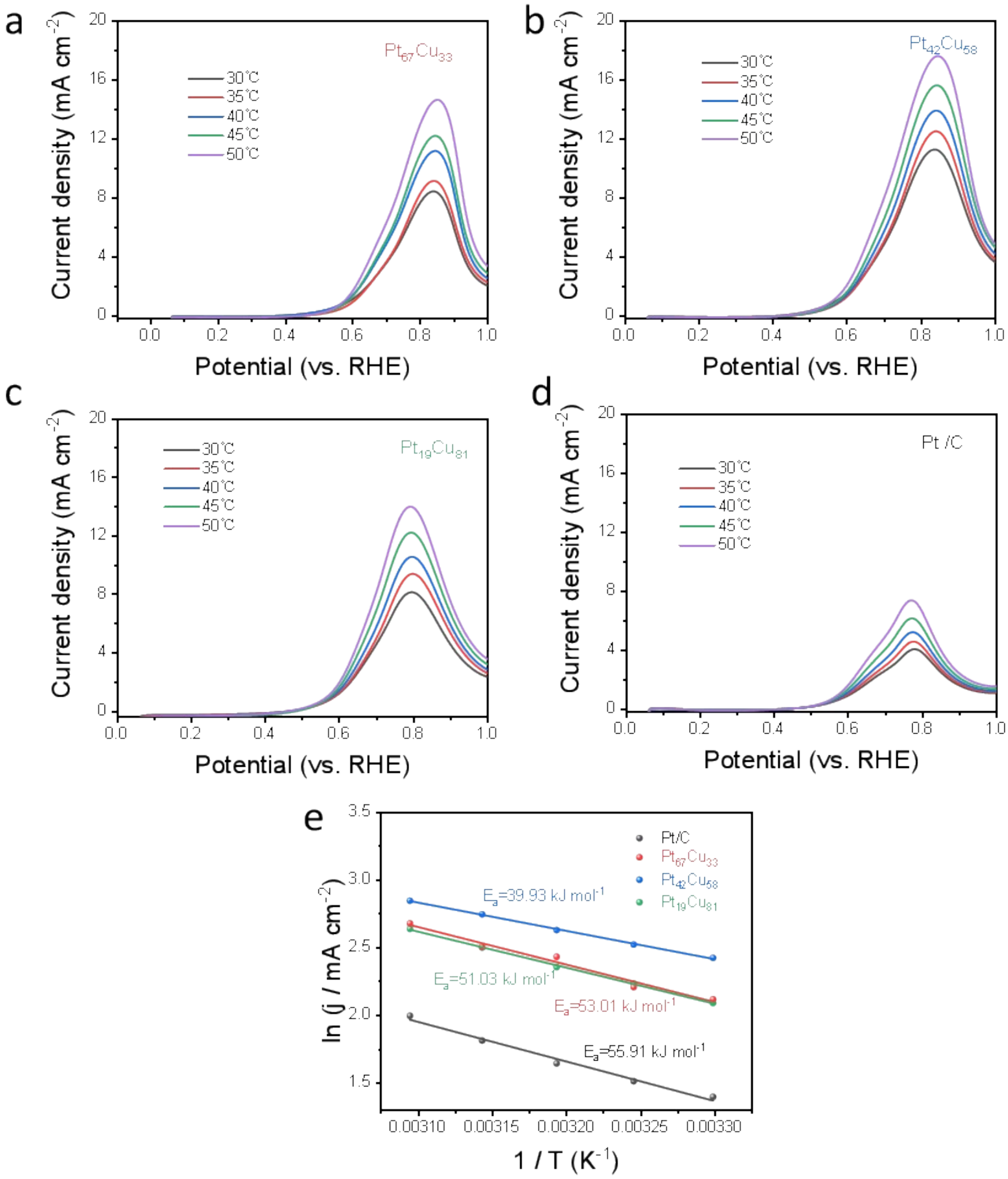

Figure S18. (a–d) LSV curves of all samples in N_2-saturated 0.1 M $HClO_4$ containing 0.5 M methanol solution electrolyte at a 50 mV s^{-1} scan rate at different temperatures (30, 35, 40, 45, and 50 °C). (e) Corresponding Arrhenius plots.

Table S1. The compositions of the Pt_xCu_y NWNs by ICP-OES

Sample	Pt (%)	Cu (%)
$Pt_{67}Cu_{33}$	67	33
$Pt_{42}Cu_{58}$	42	58
$Pt_{19}Cu_{81}$	19	81

Table S2. Lattice parameter and lattice strain of Pt_xCu_y NWNs derived from XRD patterns

Sample	2 Theta (°)	Lattice parameter (nm)	Lattice strain (%)
Pt	39.76	0.3923	/
$Pt_{67}Cu_{33}$	40.84	0.3823	-2.7254
$Pt_{42}Cu_{58}$	41.10	0.3809	-3.0633
$Pt_{19}Cu_{81}$	41.34	0.3778	-3.8514

Table S3. Calculation of Pt 5d holes using the Pt L_3-edge XANES whitelines

Samples	A_3	A_2	$h_{5d5/2}$	$h_{5d3/2}$	h_{5d}	Δh
Pt	3.83	2.18	0.602	0.398	1.000	
Pt_3Ni	3.60	1.90	0.571	0.347	0.917	-0.083
PtNi	3.47	1.79	0.551	0.327	0.878	-0.122
$PtNi_3$	3.36	1.69	0.535	0.308	0.843	-0.157
$Pt_{67}Cu_{33}$	3.19	1.50	0.511	0.274	0.785	-0.215
$Pt_{42}Cu_{58}$	3.15	1.46	0.505	0.266	0.771	-0.229
$Pt_{19}Cu_{81}$	3.07	1.37	0.494	0.251	0.745	-0.255

Table S4. Structural parameters of the Pt_xCu_y NWNs and Pt foil extracted from EXAFS fitting (S_0^2=0.81).

Sample	shell	CN	R(Å)	$\sigma^2\times10^3$(Å^2)	ΔE_0(eV)	R factor
Pt foil	Pt-Pt	12	2.765 ± 0.002	4.6 ± 0.2	7.7 ± 0.5	0.003
$Pt_{67}Cu_{33}$	Pt-Cu	2.4 ± 0.9	2.660 ± 0.013	9.0 ± 2.8	6.3 ± 0.8	0.010
	Pt-Pt	5.0 ± 1.0	2.718 ± 0.006	5.1 ± 0.7		
$Pt_{42}Cu_{58}$	Pt-Cu	4.1 ± 1.1	2.654 ± 0.010	9.0 ± 2.1	7.5 ± 0.9	0.011
	Pt-Pt	5.0 ± 1.2	2.704 ± 0.008	5.8 ± 1.1		
$Pt_{19}Cu_{81}$	Pt-Cu	2.5 ± 1.6	2.632 ± 0.014	9.3 ± 2.8	5.9 ± 1.6	0.015
	Pt-Pt	3.8 ± 1.3	2.703 ± 0.014	5.0 ± 1.9		

S_0^2: Amplitude reduction factor (obtained by fitting Pt foil);

CN: Coordination number (proportional to the intensity of k^2-FT-$\chi(k)$ peak);

R: Interatomic distance (Pt–Pt bond length);

σ^2: Debye-Waller factor (thermal and static disorder in absorber-scatterer distances);

ΔE_0: Edge energy shift (the difference between the zero kinetic energy value of the sample and that of the standard theoretical model);

R factor: Goodness of fitting (the closer the R factor is to 0.02, the more reliable the fitting outcome is).

Table S5. The performance comparison of the $Pt_{42}Cu_{58}$ NNWs catalyst with various Pt-based catalysts toward MOR.

Sample	Electrolyte	Mass Activity ($A\ mg_{Pt}^{-1}$)	Specific Activity ($mA\ cm^{-2}$)	Ref.
PtCu NNWs	0.1 M $HClO_4$ + 0.5 M methanol	1.33	4.23	This Work
PtAu NWs	0.1 M $HClO_4$ + 1.0 M methanol	1.04	3.28	12
PtRuCu NFs	0.1 M $HClO_4$ + 0.5 M methanol	0.815	7.65	13
Pt_3Cu NBs	0.5 M H_2SO_4 + 1.0 M methanol	0.533	3.10	14
E-Pt_1Ag_2 NFs/C	0.1 M $HClO_4$ + 0.5 M methanol	1.136	non	15
PtCo CNCs	0.5 M H_2SO_4 + 1.0 M methanol	0.692	3.04	16
PtRhNiCoFeGaW HEA	0.5 M H_2SO_4 and 2 M methanol	1.34	4.43	17
PtRu/C-JH	0.1 M $HClO_4$ + 1.0 M methanol	0.7059	0.5941	18
PtRuNi/C	0.5 M H_2SO_4 + 1.0 M methanol	0.844	1.93	2
PtTe PNCs	0.5 M H_2SO_4 + 1.0 M methanol	1.02	0.98	19
rugged PtCu NWs	0.5 M H_2SO_4 + 1.0 M methanol	1.03	4.39	20
PtRuAgTe NTs	0.1 M $HClO_4$ + 0.5 M methanol	1.1145	1.82	21
PtCuRh RDND	0.5 M H_2SO_4 + 1.0 M methanol	0.98	3.01	22
PtRu NWs	0.1 M $HClO_4$ + 0.5 M methanol	0.82	1.16	23
$PtCu_3$/C	0.5 M H_2SO_4 + 1.0 M methanol	1.2	3.323	24
PtFeCoNiCu HEA-700	0.1 M $HClO_4$ + 0.5 M methanol	1.4	3.29	25

PtCo MNTs	0.5 M H_2SO_4 + 1.0 M methanol	0.95	1.92	26

Table S6. A summary of MOR kinetic parameters of all samples.

Sample	Tafel slope (mV dec^{-1})	Exchange current (mA cm^{-2})	Charge transfer coefficient
Pt/C	136.39	0.59	0.43
$Pt_{67}Cu_{33}$	111.88	0.66	0.52
$Pt_{42}Cu_{58}$	84.50	0.71	0.69
$Pt_{19}Cu_{81}$	111.14	0.65	0.53

References

1. B. Ravel and M. Newville, ATHENA, ARTEMIS, HEPHAESTUS: data analysis for X-ray absorption spectroscopy using IFEFFIT, *J. Synchrotron Radiat.*, 2005, **12**, 537-541.
2. T. T. Huynh, Q. Huynh, Q. V. Nguyen and H. Q. Pham, Lattice Strain and Composition Effects on the Methanol Oxidation Performance of Platinum–Ruthenium–Nickel Ternary Nanocatalysts, *Inorg. Chem.*, 2023, **62**, 20477-20487.
3. T. T. Huynh, Q. Huynh, A. Q. K. Nguyen and H. Q. Pham, Strong Component-Interaction in N-doped 2D $Ti_3C_2T_x$-Supported Pt Electrocatalyst for Acidic Ethanol Oxidation Reaction, *Adv. Sustainable Syst.*, 2025, DOI: 10.1002/adsu.202400995.
4. M. Li, Y. Wang, J. Cai, Y. Li, Y. Liu, Y. Dong, S. Li, X. Yuan, X. Zhang and X. Dai, Surface sites assembled-strategy on Pt–Ru nanowires for accelerated methanol oxidation, *Dalton Trans.*, 2020, **49**, 13999-14008.
5. K. Peng, N. Bhuvanendran, S. Ravichandran, W. Zhang, Q. Ma, Q. Xu, L. Xing, L. Khotseng and H. Su, Bimetallic Pt3Mn nanowire network structures with enhanced electrocatalytic performance for methanol oxidation, *Int. J. Hydrogen Energy*, 2020, **45**, 30455-30462.
6. B. Luo, F. Zhao, Z. Xie, Q. Yuan, F. Yang, X. Yang, C. Li and Z. Zhou, Polyhedron-Assembled Ternary PtCuCo Nanochains: Integrated Functions Enhance the Electrocatalytic Performance of Methanol Oxidation at Elevated Temperature, *ACS Appl. Mater. Interfaces*, 2019, **11**, 32282-32290.
7. Y. Zheng, A. S. Petersen, H. Wan, R. Hübner, J. Zhang, J. Wang, H. Qi, Y. Ye, C. Liang, J. Yang, Z. Cui, Y. Meng, Z. Zheng, J. Rossmeisl and W. Liu, Scalable and Controllable Synthesis of Pt-Ni Bunched-Nanocages Aerogels as Efficient Electrocatalysts for Oxygen Reduction Reaction, *Adv. Energy Mater.*, 2023, **13**, 2204257.
8. S. Wang, T. Sheng and Q. Yuan, Low-Pt Octahedral PtCuCo Nanoalloys: "One Stone, Four Birds" for Oxygen Reduction and Methanol Oxidation Reactions, *Inorg. Chem.*, 2023, **62**, 11581-11588.
9. L. F. Mattheiss and R. E. Dietz, Relativistic tight-binding calculation of core-valence transitions in Pt and Au, *Phys. Rev. B*, 1980, **22**, 1663-1676.
10. D. Wang, X. Cui, Q. Xiao, Y. Hu, Z. Wang, Y. M. Yiu and T. K. Sham, Electronic behaviour of Au-Pt alloys and the 4f binding energy shift anomaly in Au bimetallics- X-ray spectroscopy studies, *AIP Adv.*, 2018, **8**, 065210.
11. J. Chen, Y. M. Yiu, Z. Wang, D. Covelli, R. Sammynaiken, Y. Z. Finfrock and T.-K. Sham, Elucidating the Many-Body Effect and Anomalous Pt and Ni Core Level Shifts in X-ray Photoelectron Spectroscopy of Pt–Ni Alloys, *J. Phys. Chem. C*, 2020, **124**, 2313-2318.
12. Y. Liu, E. Zhu, J. Huang, A. Zhang, A. H. Shah, Q. Jia, M. Xu, E. Liu, Q. Sun, X. Duan and Y. Huang, Periodic Assembly of Diblock Pt–Au Heteronanowires for the Methanol Oxidation Reaction, *Nano Lett.*, 2023, **23**, 2758-2763.
13. M. Qiao, F. Y. Meng, H. Wu, Y. Wei, X. F. Zeng and J. X. Wang, PtCuRu Nanoflowers with Ru-Rich Edge for Efficient Fuel-Cell Electrocatalysis, *Small*, 2022, **18**, 2204720.

14. Z. Zhang, J. Li, S. Liu, X. Zhou, L. Xu, X. Tian, J. Yang and Y. Tang, Self-Templating-Oriented Manipulation of Ultrafine Pt_3Cu Alloyed Nanoparticles into Asymmetric Porous Bowl-Shaped Configuration for High-Efficiency Methanol Electrooxidation, *Small*, 2022, **18**, 2202782.
15. M. Qiao, H. Wu, F. Y. Meng, Z. Zhuang and J. X. Wang, Defect-Rich, Highly Porous PtAg Nanoflowers with Superior Anti-Poisoning Ability for Efficient Methanol Oxidation Reaction, *Small*, 2022, **18**, 2106643.
16. Z. Li, X. Jiang, X. Wang, J. Hu, Y. Liu, G. Fu and Y. Tang, Concave PtCo nanocrosses for methanol oxidation reaction, *Appl. Catal., B*, 2020, **277**, 119135.
17. F. Si, S. Wang, Y. Zhang, R. Xue, Y. Lv, G. Chen and D. Gao, Lattice distortion and elemental synergy in platinum-based high-entropy alloy boosts liquid fuels electrooxidation, *Chem. Eng. J.*, 2024, **494**, 153213.
18. Y. Deng, H. Liu, L. Lai, F. She, F. Liu, M. Li, Z. Yu, J. Li, D. Zhu, H. Li, L. Wei and Y. Chen, Platinum-Ruthenium Bimetallic Nanoparticle Catalysts Synthesized Via Direct Joule Heating for Methanol Fuel Cells, *Small*, 2025, **21**, 2403967.
19. Q. Zhang, T. Xia, H. Huang, J. Liu, M. Zhu, H. Yu, W. Xu, Y. Huo, C. He, S. Shen, C. Lu, R. Wang and S. Wang, Autocatalytic reduction-assisted synthesis of segmented porous PtTe nanochains for enhancing methanol oxidation reaction, *Nano Research Energy*, 2023, **2**, e9120041.
20. L. Huang, W. Zhang, Y. Zhong, P. Li, D. Xiang, W. Uddin, X. Li, Y.-G. Wang, X. Yuan, D. Wang and M. Zhu, Surface-structure tailoring of ultrafine PtCu nanowires for enhanced electrooxidation of alcohols, *Sci. China Mater.*, 2020, **64**, 601-610.
21. Q.-X. Chen, C.-X. Yu, H.-H. Li, Z. He and J.-W. Liu, Composition Modulation of Pt-Based Nanowire Electrocatalysts Enhances Methanol Oxidation Performance, *Inorg. Chem.*, 2020, **59**, 1376-1382.
22. Z. Wang, L. Huang, Z. Q. Tian and P. K. Shen, The controllable growth of PtCuRh rhombic dodecahedral nanoframes as efficient catalysts for alcohol electrochemical oxidation, *J. Mater. Chem. A*, 2019, **7**, 18619-18625.
23. L. Huang, X. Zhang, Q. Wang, Y. Han, Y. Fang and S. Dong, Shape-Control of Pt–Ru Nanocrystals: Tuning Surface Structure for Enhanced Electrocatalytic Methanol Oxidation, *J. Am. Chem. Soc.*, 2018, **140**, 1142-1147.
24. Z. Xing, J. Li, S. Wang, C. Su and H. Jin, Structure engineering of PtCu3/C catalyst from disordered to ordered intermetallic compound with heat-treatment for the methanol electrooxidation reaction, *Nano Res.*, 2022, **15**, 3866-3871.
25. D. Wang, Z. Chen, Y.-C. Huang, W. Li, J. Wang, Z. Lu, K. Gu, T. Wang, Y. Wu, C. Chen, Y. Zhang, X. Huang, L. Tao, C.-L. Dong, J. Chen, C. V. Singh and S. Wang, Tailoring lattice strain in ultra-fine high-entropy alloys for active and stable methanol oxidation, *Sci. China Mater.*, 2021, **64**, 2454-2466.
26. S. Yin, Z. Wang, X. Qian, D. Yang, Y. Xu, X. Li, L. Wang and H. Wang, PtM (M = Co, Ni) Mesoporous Nanotubes as Bifunctional Electrocatalysts for Oxygen Reduction and Methanol Oxidation, *ACS Sustainable Chem. Eng.*, 2019, **7**, 7960-7968.